

# Imaging of Laser-induced Plasma Expansion Dynamics in Ambient Air

**GHANESHWAR GAUTAM, CHRISTOPHER M. HELSTERN, KYLE A. DRAKE AND  
CHRISTIAN G. PARIGGER\***

*The University of Tennessee / UT Space Institute, Center for Laser Applications,  
411 B.H. Goethert Parkway, Tullahoma, TN 37388-9700, USA*

\*Corresponding author E-mail address: cparigge@tennessee.edu (C.G. Parigger)

**ABSTRACT:** Laser-induced plasma is generated with 6-ns, 800-mJ Nd:YAG 1064-nm laser radiation in standard ambient temperature and pressure air. The expansion dynamics are explored using synchronized, 532-nm laser pulses from a second Nd:YAG laser device. Shadowgraphs are recorded during the first 4 microseconds to visualize the expansion dynamics. The detailed experimental records show density variations consistent with Abel inverted spectra.

**PACS Codes:** 52.27.-h, 52.35.Tc, 52.38.-r, 47.40.Nm, 87.63.It, 87.63.L-

**Key Words:** Plasma dynamics and flow, shock waves and discontinuities, laser-plasma interactions, Shock wave interactions and shock effects in fluid dynamics, laser imaging, visual imaging, air, plasma diagnostics, laser-induced optical breakdown

## 1. INTRODUCTION

The generation of laser-induced optical breakdown with nanosecond Nd:YAG 1064-nm laser radiation causes hypersonic shock waves that typically reduce to supersonic speeds of Mach number,  $Ma = 3$ , at time delays of the order of 1 microsecond. Fluid dynamics effects can be measured for time delays several orders of magnitude longer than the deposition of energy during the pulse width [1-3]. The expansion dynamics can be visualized using high-speed photography [4-6], or they can be investigated using optical emission spectroscopy (OES) and Abel inversion [7-12]. However, in view of the electron density variation along the line-of-sight of the laser plasma, a detailed collection of shadowgraphs is recorded that support the Abel inversion results.

The measurement and analysis of organic and inorganic gaseous, liquid or solid materials following optical breakdown is known as laser-induced breakdown spectroscopy (LIBS). This technique allows one to measure composition with a minimally invasive approach [13]. Some current applications of LIBS include the detection of biological contaminants on foods [14], polymer identification for recycling of different hazardous types of plastics [15], liquid slag analysis for steel production [16], and lunar exploration [17]. Plasma radiation is usually recorded in LIBS in a line-of-sight arrangement using time-resolved spectroscopy [18].

The shadowgraph technique is based on the variation of the refractive index causing refraction of the light used for imaging. Changes of the index of refraction directly correspond to the light and dark records in the data. In schlieren analysis, a knife edge is used to cut off directly propagating optical radiation to capture the deflected light; however, shadowgraph and schlieren techniques are closely related [19, 20]. The schlieren method is based on the transverse derivative for the image formation, and shadowgraphy relies on the Laplacian or second derivative. Shadowgraphs have been extensively used in fluid flow visualization and are equally applicable in shockwave analysis of laser-induced plasma. When collimated laser light passes the area of interest with a varying refractive

index, the light rays are refracted and a shadow pattern that is projected onto a screen can be recorded with a standard camera or charge-coupled device (CCD). Measurements of shadowgraphs are applied in different fields of research including aerodynamics and fluid mechanics [21-25], medical and industrial applications [26, 27].

Here, the shadowgraph technique is used to observe the density gradient and shock-wave formation in transient plasma. The non-uniformities in the plasma expansion can be recorded with high-speed photography realized using short pulses from another laser device. Shadowgraphy allows one to visualize the abrupt changes in gaseous and laser-plasma generated shock waves. Valuable time-resolved information about the laser-matter interaction can be obtained from analysis of the shock wave. Higher density regions of the plasma appear comparatively darker than its surrounding parts indicating partial blockage of light rays. The detailed images serve as a guide for spectroscopic analysis including computer tomographic methods. The shockwave indicates higher values of electron density and temperature in that region of the plasma.

## 2. EXPERIMENTAL DETAILS FOR SHADOWGRAPH IMAGING

A Quantel laser device (model Q-smart 850) is operated at its fundamental wavelength of 1064 nm, 6 ns pulse width, 850 mJ per pulse energy to induce optical breakdown. In addition, a Quanta Ray laser operated at its second harmonic wavelength of 532 nm with a pulse width of 17 ns and energy of up to 120 mJ per pulse. Figure 1 illustrates the experimental arrangement.

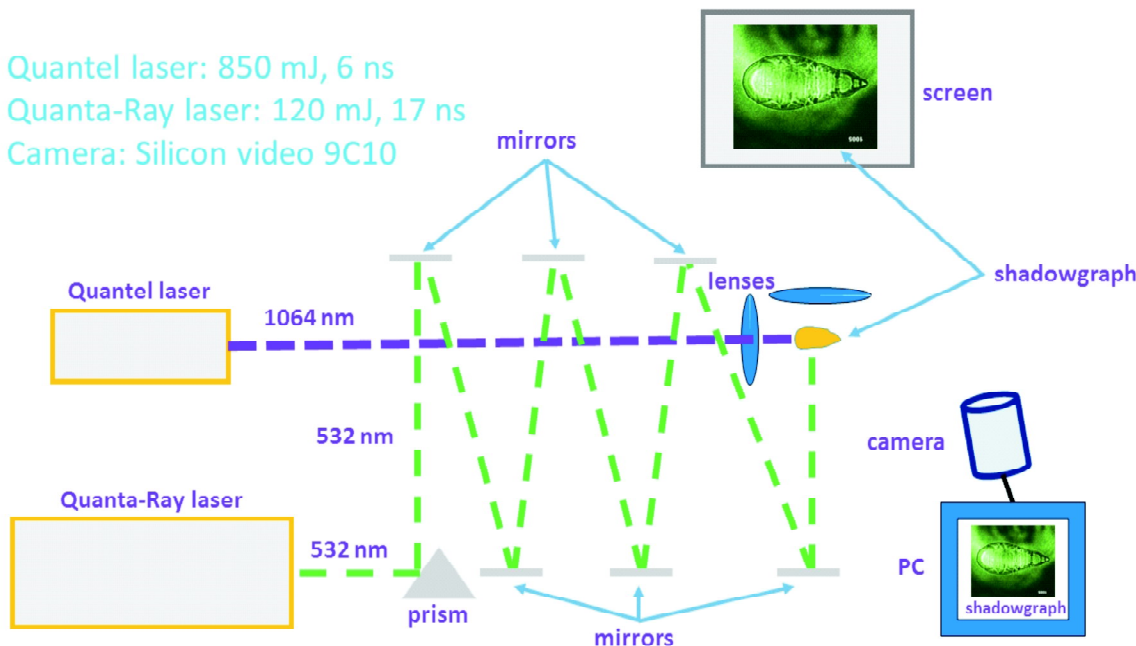


Figure 1: Schematic of the shadowgraph experiment in laboratory air

The 1064-nm IR beam is focused with a 100 mm plano convex lens, f/10 focusing is used. The peak irradiance in focus would amount to  $50 \text{ TW/cm}^2$  which is over 2 orders of magnitude above the threshold of  $\sim 0.3 \text{ TW/cm}^2$  required for air breakdown at standard ambient temperature and pressure (SATP). The 532-nm green laser beam is reflected by a prism perpendicular to the original beam direction, which emerges from the laser source and is used to cast a shadowgraph of the plasma after multiple reflection from six mirrors. In the initial setup, a six-mirror, variable optical delay line up to 32 m served the purpose of exploring shadowgraphs with a single laser device. However, electronic synchronization is the preferred method for the recording of shadowgraphs up to 4  $\mu\text{s}$  time delay. The selected distance between each mirror is 1.2 m with a total optical path of 8 m. The green beam slightly

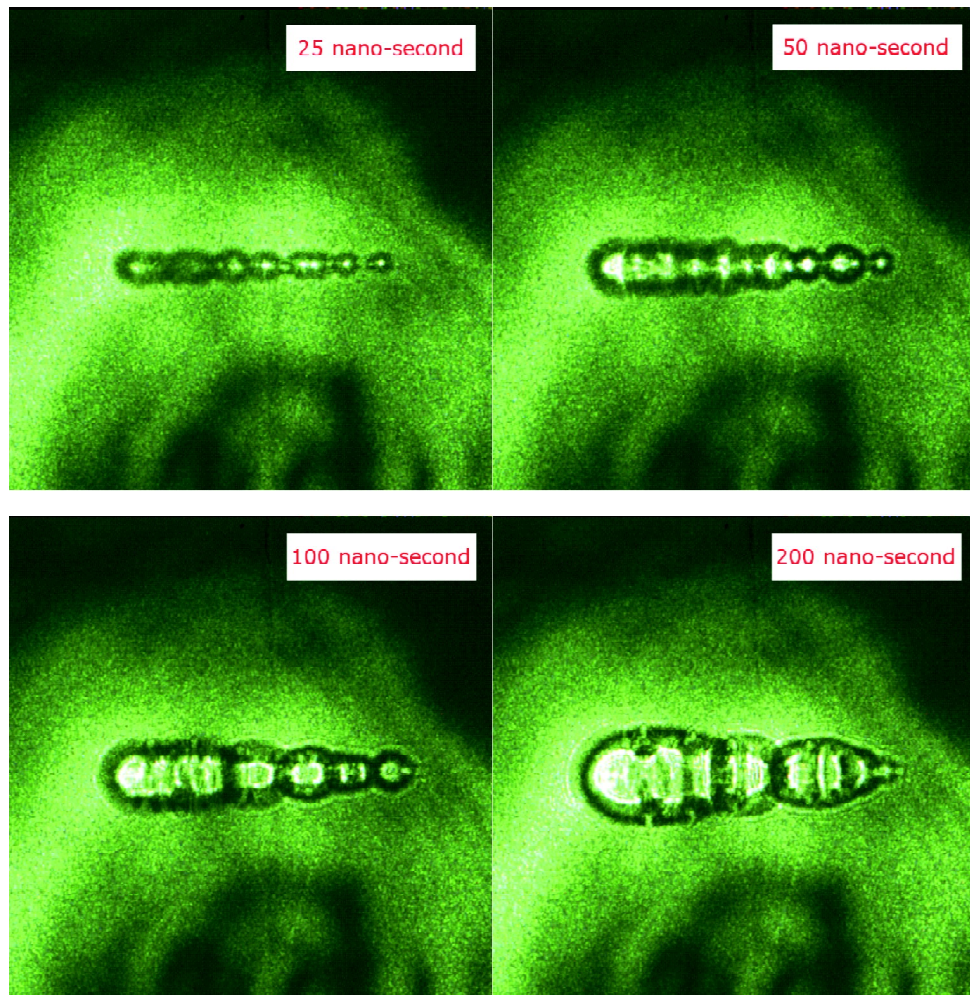
expands along the 8 m optical path and becomes sufficiently wide to nicely cover the plasma volume for shadowgraph imaging.

The two lasers and camera were synchronized for accurate temporal measurements of the shadowgraphs. A function generator (Wavetek FG3C), digital delay generator (Stanford Research System DG535) and a custom built divide-by-five box were also used in the electronic synchronization process following similar procedures previously utilized [28]. The trigger jitter of the externally controlled Quanta Ray laser amounted to  $\pm 1$  ns RMS amplitude. The indicated image lens in the figure is used to obtain a shadowgraph magnification of 20:1 on the screen.

A Silicon video 9C10 camera with a Nikon lens of 50 mm focal length was employed to record shadowgraph images directly from the screen without the use of a narrowband, green filter. The 9C10 video camera has a 6.1 mm  $\times$  4.58 mm sensitive area with square  $1.75 \mu\text{m} \times 1.75 \mu\text{m}$  pixels, or a resolution of 3488 horizontal  $\times$  2616 vertical pixels. The images were recorded using  $4 \times 4$  grouping and an overall image resolution of  $512 \times 512$  pixels. XCAP imaging software with a PIXCI image capture board was available to control the Silicon video CMOS based camera.

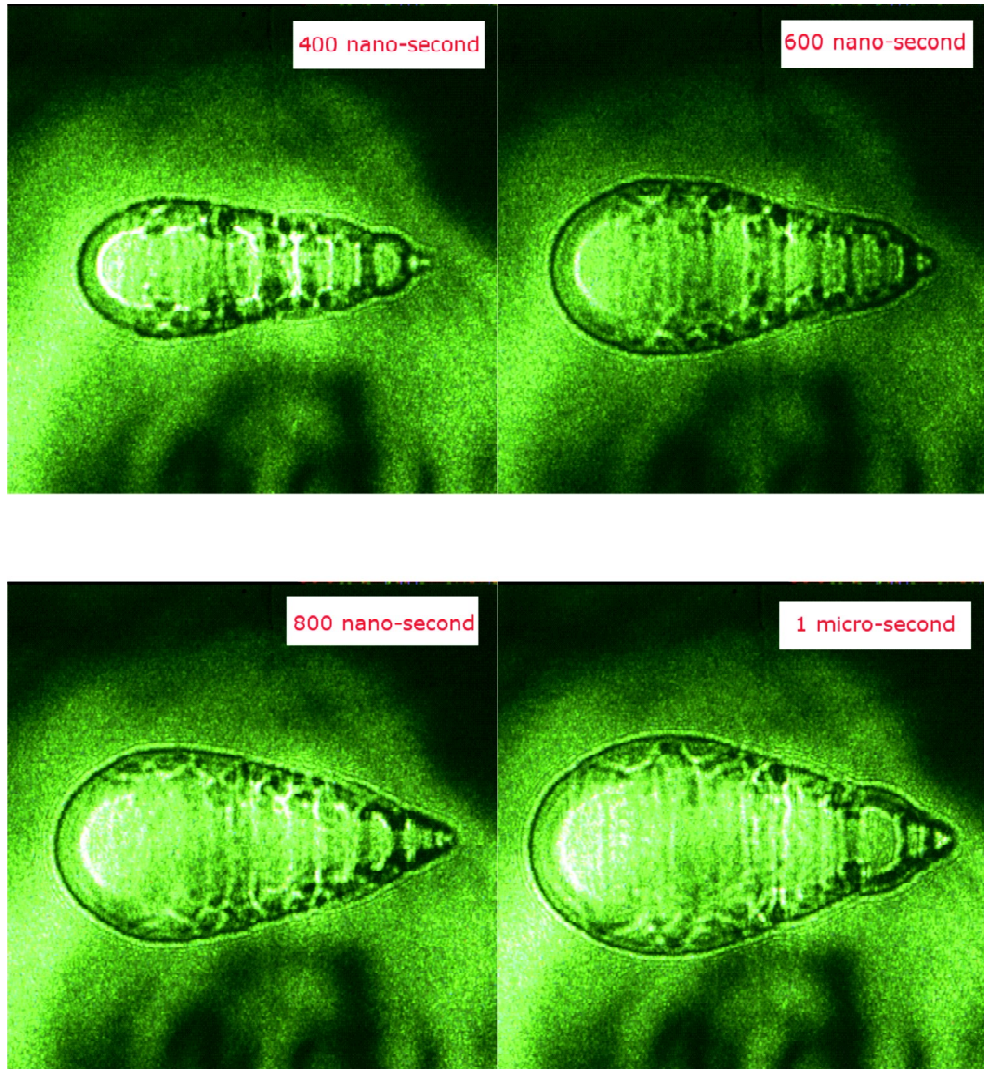
### 3. RESULTS AND DISCUSSION

Figure 2 displays typical recorded results of the shadowgraphs for the time delays of 25 to 200 ns. The laser beam is focused from left to right and optical breakdown occurs as the threshold irradiance is reached. The images show an area of 12.7 mm  $\times$  12.7 mm.



**Figure 2: Shadowgraphs during the first 200 ns after optical breakdown**

These two-dimensional images represent the expansion of the plasma along with corresponding shock waves that emanate parallel and perpendicular to the laser beam propagation direction. At 25 ns time delay, multiple optical breakdown spots are seen. The whole plasma shape is close to a cylindrical shape and it appears that there are many bubbles connected together. This close to cylindrical plasma shape changes to a spherical shape for later time delays specifically toward the laser beam direction. The greenish-gray color outside the white centers indicates the initiation of shock waves from these breakdown spots, and white areas inside the shock waves are the low density regions where more light passes than in the surrounding area. Figure 3 illustrates images recorded for time delays of 400 ns to 1  $\mu$ s.



**Figure 3: Shadowgraphs showing the laser-plasma expansion from 400 ns to 1  $\mu$ s**

The shock wave is generated when the fast moving plasma plume pushes the gas pile-up outward. The faint lines outside the shock wave are the result of diffraction effects of the shock wave. Successive lines from the shock wave correspond to 1<sup>st</sup> and 2<sup>nd</sup> order diffraction patterns, respectively. These lines are more visible for later time delays, i.e., for 1  $\mu$ s in Fig. 3.

Furthermore, stagnation layers are developed inside the plasma due to the interaction of two or more optical breakdown events that originate from different spots along the optical axis as elucidated in Figure 2. The dark area above and below the shadowgraphs are reminiscent of the imaging laser beam profile. When using nanosecond

laser pulses with peak irradiances well above optical breakdown threshold, most of the laser pulse interacts or couples with the plasma resulting in a laser-driven expansion and shock wave. This laser-plasma interaction depends on the plasma frequency and electron density,  $n_e$ . For  $n_e < 10^{21}/\text{cm}^3$ , the 1064-nm excitation laser beam is fully absorbed once optical breakdown is achieved. The development of the laser-supported plasma reveals primarily spherical symmetry for the expansion of the “bubble” towards the laser side (left in the images). Fig. 4 shows the recorded images for time delays of 1.5 to 4  $\mu\text{s}$ .

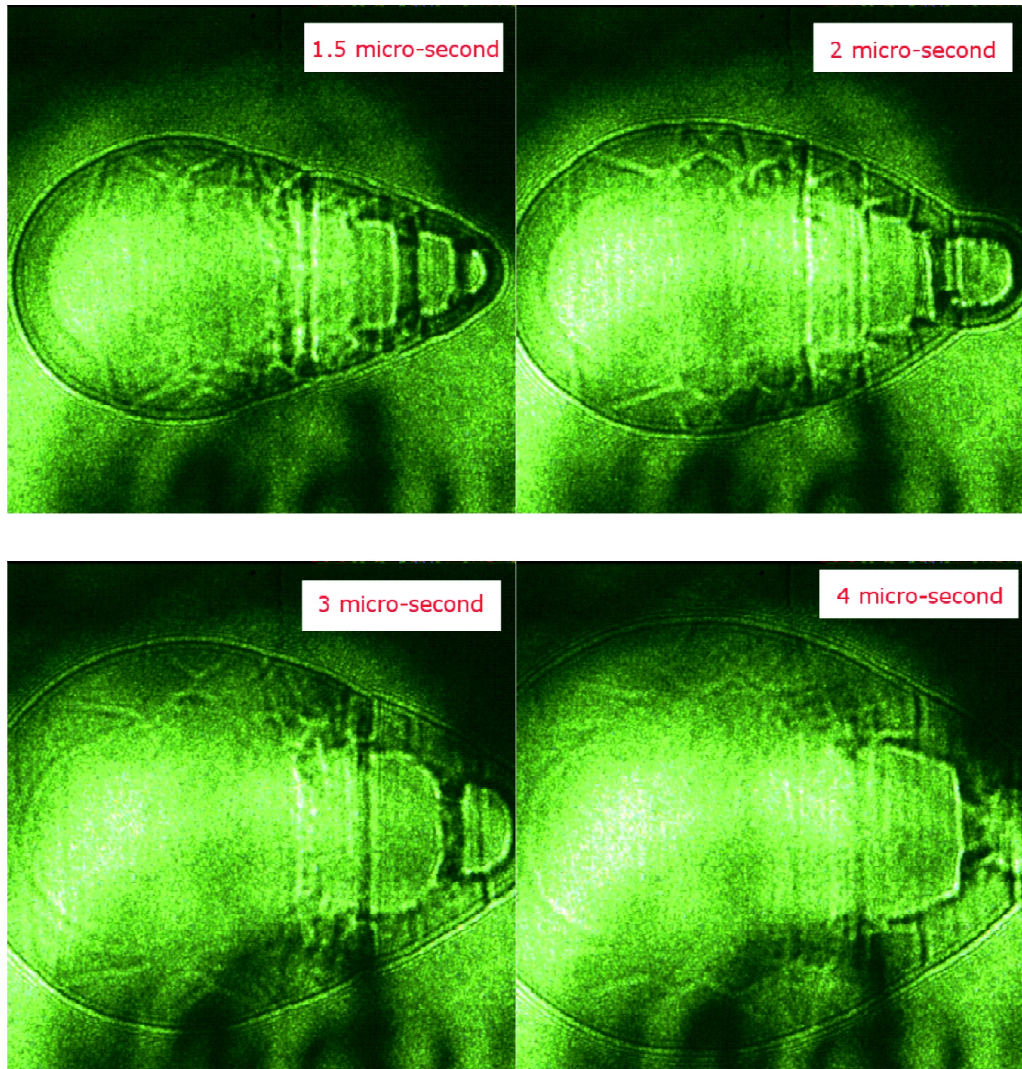


**Figure 4: Shadowgraphs of the plasma for time delays of 1.5 to 4  $\mu\text{s}$**

The displayed images in Figures 2 to 4 were originally recorded in red-green-blue (RGB) colors and stored as tagged-image-files (TIF) but are converted to PNG files and labeled using Gimp 2.8 software. These images can also be transferred to gray scale color. However, gray scale images reproduce similar quality shadowgraphs.

The expanding plasma grows to a larger diameter towards the laser side (left in the images) than in the forward direction. Each individual breakdown spot shows close to spherical expansion yet the overall plasma shape appears to be close to cylindrical during the early time delays. For later time delays, Figs. 3 and 4 indicate a close to spherical shape especially towards the laser side due to the laser-supported absorption following optical breakdown.

The Taylor-Sedov theory of blast wave propagation from a point explosion yields the time dependent radius,  $R(t)$ , of the shock front [27, 29, 30],

$$R(t) = \xi(E/\rho)^{\frac{1}{n+2}}(t)^{\frac{2}{n+2}} \sim (t)^{\frac{2}{n+2}}. \quad (1)$$

Here,  $\xi$  is a constant in the range of 1 to 1.1 that depends on the specific heat capacity,  $E$  is the energy released during the explosion or the absorbed energy per laser pulse,  $\rho$  is the gas density,  $t$  is the time delay and  $n$  is the shape dependent parameter. The values of  $n = 1, 2, 3$  correspond to planar, cylindrical and spherical shock waves, respectively.

One can use Equation (1) to calculate the blast wave or shock front expansion generated from laser-induced optical breakdown. However, of primary interest is the dependence of the radius,  $R(t)$  on time delay,  $t$ . Figure 5 displays the maximum of the shock wave radius versus time delay measured perpendicular to the direction of the laser beam propagation.

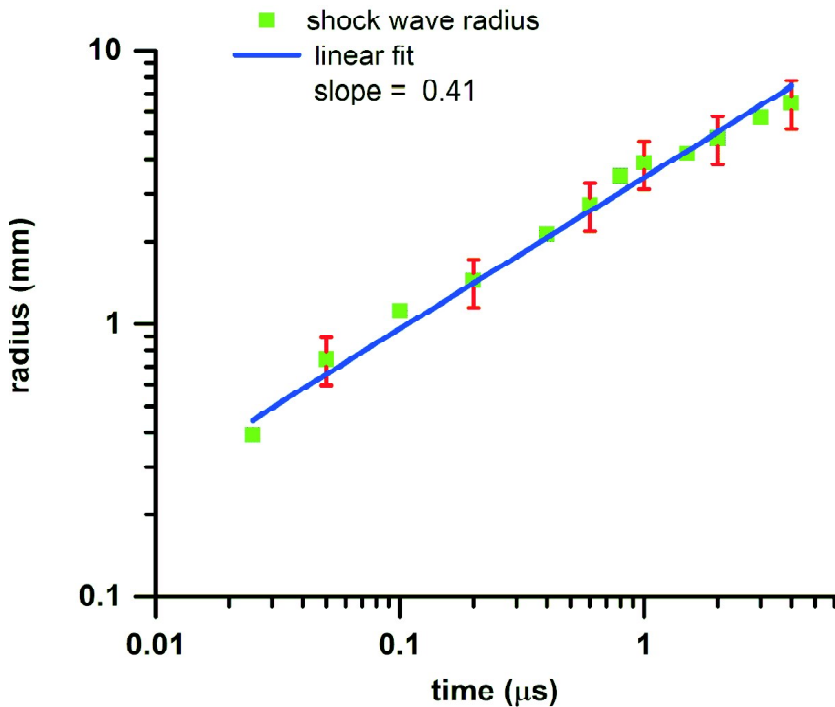


Figure 5: Log-log plot of shock wave expansion perpendicular to the laser-propagation direction

The linear fit reveals 0.41 for the slope, or  $n = 2.9 \sim 3$ . In other words, spherical expansion is inferred. The figure also shows 20% error bars. These error bars are estimated from the variations in the pulse energy for generation of optical breakdown, the trigger-jitter synchronization of the two laser beams, and the readout errors from the displayed images in Figs. 2 to 4. One can also extract from the graph the approximate 1 mm per  $\mu\text{s}$  expansion velocity for time delays of  $\sim 1\mu\text{s}$ , or  $\text{Ma} = 3$ . From Equation (1), using  $\xi = 1.0$  to  $1.1$ ,  $E = 800 \text{ mJ}$ ,  $\rho = 1.225 \text{ kg/m}^3$  and  $n = 3$  yields for the radius  $R(t = 1 \mu\text{s}) = 3.7$  to  $4.1 \text{ mm}$ , consistent with the measured value of  $3.9 \text{ mm}$ .

#### 4. CONCLUSIONS

The recorded shadowgraphs indicate multiple epicenters of laser-plasma generation. Laser-induced optical breakdown is generated with focused laser radiation that can reach peak irradiances well above thresholds. The laser-supported blast wave shows a spherical expansion and is due to absorption of most of the pulse energy in the region towards

the laser. Lesser amount of energy absorption occurs in the forward direction. The colliding shockwaves from multiple breakdown spots cause stagnation layers that tend to disappear on the laser side for longer time delays but tend to prevail in the forward direction.

Most importantly, the symmetric images along the optical axis indicate higher electron densities near the shockwave front. Higher electron density would imply higher electron temperature in these regions as well, consistent with previous results inferred from Abel inverted, time-resolved emission spectra that were recorded during plasma expansion in air.

### Acknowledgments

The authors acknowledge support in part for this work by the Accomplished Center of Excellence, Center for Laser Applications (CLA) at the University of Tennessee Space Institute (UTSI) and thank for comments from Ashraf M. El Sherbini.

### References

- [1] A. W. Mizolek, V. Palleschi, I. Schechter, *Laser-Induced Breakdown Spectroscopy*, Cambridge University Press, NY, 2006.
- [2] L. J. Radziemski, D. A. Cremers, *Laser-Induced Plasmas and Applications*, M. Dekker, NY, 1989.
- [3] I. G. Dors, C. G. Parigger, *Appl. Opt.* **42** (2003) 5978.
- [4] G. S. Settles, *Schlieren and Shadowgraph Techniques*, Springer-Verlag, NY, 2012.
- [5] M. Thiyagarajan, K. Williamson, A. R. Kandi, *IEEE Trans. Plasma Sci.* **40** (2012) 2491.
- [6] M. Thiyagarajan, S. Thompson, *J. Appl. Phys.* **111** (2012) 073302.
- [7] G. Pretzler, H. Jäger, T. Neger, H. Philipp, J. Woisetschläger, *Z. Naturforsch.* **47a** (1992) 955.
- [8] A. S. Merk, S. V. Shabanov, I. B. Gornushkin, U. Panne, *J. Anal. At. Spectrom.* **26** (2011) 2483.
- [9] C. G. Parigger, G. Gautam, D. M. Surmick, *Int. Rev. At. Mol. Phys.* **6** (2015) 43.
- [10] G. Gautam, C. G. Parigger, *Int. Rev. At. Mol. Phys.* **6** (2015) 83.
- [11] S. Eschlböck-Fuchs, A. Demidov, I. B. Gornushkin, T. Schmid, R. Rössler, N. Huber, U. Panne, J. D. Pedarnig, *Spectrochim. Acta Part B* **123** (2016) 59.
- [12] C. G. Parigger, D. M. Surmick, G. Gautam, Self-absorption characteristics of measured laser-induced plasma line shapes, *J. Phys.: Conf. Ser.* **810** (2017) 012012.
- [13] R. Noll, *Laser-Induced Breakdown Spectroscopy: Fundamentals and Applications*, Springer, Berlin, 2012.
- [14] R. A. Multari, D. A. Cremers, J. A. M. Dupre, J. E. Gustafson, *J. Agric. Food Chem.* **61** (2013) 8687.
- [15] S. Grégoire, M. Boudinet, F. Pelascini, F. Surma, V. Detalle, Y. Holl, *Anal. Bioanal. Chem.* **400** (2011) 3331.
- [16] V. Sturm, R. Fleige, M. de Kanter, R. Leitner, K. Pilz, D. Fischer, G. Hubmer, R. Noll, *Anal. Chem.* **86** (2014) 9687.
- [17] J. Lasue, C. Wiens, S. Clegg, T. Vaniman, H. Joy, S. Humphries, A. Mezzacappa, N. Melikechi, R. McInroy, S. Bender, *J. Geophys. Res.* **117** (2012) E01002.
- [18] C. G. Parigger, G. Gautam, A. C. Woods, D. M. Surmick, J. O. Hornkohl, *Trends Appl. Spectrosc.* **11** (2014) 1.
- [19] A. Davidhazy, Introduction to shadowgraph and schlieren imaging, in Rochester Institute of Technology, RIT Scholar Works, Rochester, NY, 2006.
- [20] P. K. Panigrahi and K. Muralidhar, *Laser Schlieren and Shadowgraph, Schlieren and Shadowgraph Methods in Heat and Mass Transfer*, Springer Briefs in Thermal Engineering and Applied Science, Springer-Verlag, NY, 2012.
- [21] T. Perhavec, J. Diaci, *J. Mech. Eng.* **56** (2010) 477.
- [22] P. Gregorèi, J. Možina, *Opt. Lett.* **36** (2011) 2782.
- [23] R. Castrejón-Garæya, J.R. Castrejón-Pita, G.D. Martin, I.M. Hutchings, *Rev. Mex. Fis.* **57** (2011) 266.
- [24] X. Zeng, X. Mao, S. S. Mao, S.-B. Wen, R. Greif, R. E. Russo, *Appl. Phys. Lett.* **88** (2006) 061502.
- [25] C. G. Parigger, *Spectrochim. Acta Part B* **79-80** (2013) 4.
- [26] A. Vogel, *Phys. Med. Biol.* **42** (1997) 895.
- [27] M. Kandula, R. Freeman, *Shock Waves* **18** (2008) 21.
- [28] C.G. Parigger, A.C. Woods, M.J. Witte, L.D. Swafford, D. M. Surmick, *J. Vis. Exp.* **84** (2014) 51250.
- [29] A. E. Hussein, P. K. Diwakar, S. S. Harilal, A. Hassanein, *J. Appl. Phys.* **113** (2013) 143305.
- [30] S. S. Harilal, G. V. Miloshevsky, P. K. Diwakar, N. L. LaHaye, A. Hassanein, *Phys. Plasmas* **19** (2012) 083504.